Supporting Information

Direct Identification of Antisite Cation Intermixing and Correlation with Electronic Conduction in $CuBi_2O_4$ for Photocathodes

Hyun Joon Jung,[1,2] Younghwan Lim,[1] Byeong-Uk Choi,[1] Hyung Bin Bae,[3] WooChul Jung,[1] Sangwoo Ryu,[4] Jihun Oh,[1] and Sung-Yoon Chung[1,*]

[1]Department of Materials Science and Engineering, Korea Advanced Institute of Science and Technology, Daejeon 34141, Korea
[2]Graduate School of EEWS, Korea Advanced Institute of Science and Technology, Daejeon 34141, Korea
[3]KAIST Analysis Center, Korea Advanced Institute of Science and Technology, Daejeon 34141, Korea
[4]Department of Advanced Materials Engineering, Kyonggi University, Suwon, Gyeonggi-Do 16227, Korea

*Email: sychung@kaist.ac.kr

Experimental details

Film fabrication. Polycrystalline $CuBi_2O_4$ films were fabricated by using a sol–gel process. $Bi(NO_3)_3{\cdot}5H_2O$ (99.999%, Sigma-Aldrich) and $Cu(NO_3)_3{\cdot}2.5H_2O$ (>99.99%, Sigma-Aldrich) were used as starting materials for the preparation of a precursor solution. The bismuth nitrate (1 M) and the copper nitrate (0.5 M) were dissolved in 5-mL dimethylformamide (DMF, 99.8%, Merck) with 0.024 M polyvinyl pyrrolidone (PVP10, Sigma-Aldrich, average molecular weight = 10,000) in a ultrasonication bath to prepare a precursor solution. The precursor solution was deposited on (001) MgO and (0001) Al_2O_3 single-crystal substrates by a spin-coating method at 3000 rpm. The wet films were heat-treated at 200°C for 2 h in air and finally annealed at 550°C or 750°C for 2 h in air for crystallization. The grown films were confirmed by X-ray diffractometry (X'Pert-PRO MRD, PANalytical) with Cu-K_α radiation.

STEM, EDS, image simulations, and optical/electrical measurements . Samples for STEM observation were prepared by lift out via ion-beam milling in a focused ion beam system (Quanta 3D FEG and Helios G4 UX, Thermo Fisher Scientific). Protective amorphous carbon and thin Pt layers were applied before milling. HAADF and BF STEM images were simultaneously taken with a transmission electron microscope (Titan cubed G2 60-300, Thermo Fisher Scientific) at 300 kV with a spherical aberration (Cs) corrector (CEOS GmbH). The optimum size of the electron probe was ~1 Å with a convergence semiangle of 19 mrad. The collection semiangles of the STEM detectors were set to 79.5–200 mrad for HAADF imaging and 0–43.3 mrad for BF imaging. Chemical mapping with EDS was carried out in the Titan cubed G2 at 300 kV along with four integrated silicon-drift EDS detectors (ChemiSTEM™ technology) at a collection solid angle of 0.7 srad. Bi-M_α (2.4 keV) and Cu-K_α (8.0 keV) lines were selected during elemental mapping. The probe current was adjusted to be 50–100 pA with a scanning time of ~300 sec. The EDS maps were low-pass filtered using Bruker ESPRIT software after the reduction of background noise for better visualization. STEM image simulations in the HAADF mode were performed using QSTEM (ver. 2.22) based on the multislice method. The intensity of the HAADF images was calculated by summing the scattered electrons with collection semiangles of 79 to 200 mrad under a condition of Cs = 0 with a specimen thickens of 10 nm. The optical absorption spectra of films were acquired by using a UV/VIS/NIR spectrophotometer (Lambda 1050+, PerkinElmer) in a wave-length range of 300–1400 nm. The film resistivity with temperature was measured (Keithley 2450 SMU) as a function of temperature with thin Pt electrodes deposited by a sputtering method.

DFT calculations. *Ab initio* DFT calculations for the DOS and the electronic band structure were carried out using the spin-polarized generalized-gradient approximation (GGA) along

with the PBEsol functional revised for exchange correlation of densely packed solids and the ultrasoft pseudopotentials for ionic cores, as implemented in the CASTEP code (Biovia Inc.). To account for the electron localization around Cu^{2+} ions, the GGA + *U* method with the Hubbard *U* parameter (7.0 eV for Cu 3*d* states) was employed. The plane-wave basis set for the kinetic energy cutoff was 1000 eV for rigorous calculations. Relaxation of the internal coordinates for each atom was performed using the Broyden–Fletcher–Goldfarb–Shanno (BFGS) algorithm with convergence tolerances of 0.1 eV/Å for the maximum ionic force, 5×10^{-5} eV/atom for the total energy, and 0.005 Å for the maximum ionic displacement.

Movie S1. Three-dimensional illustration for the $CuBi_2O_4$ crystal structure.

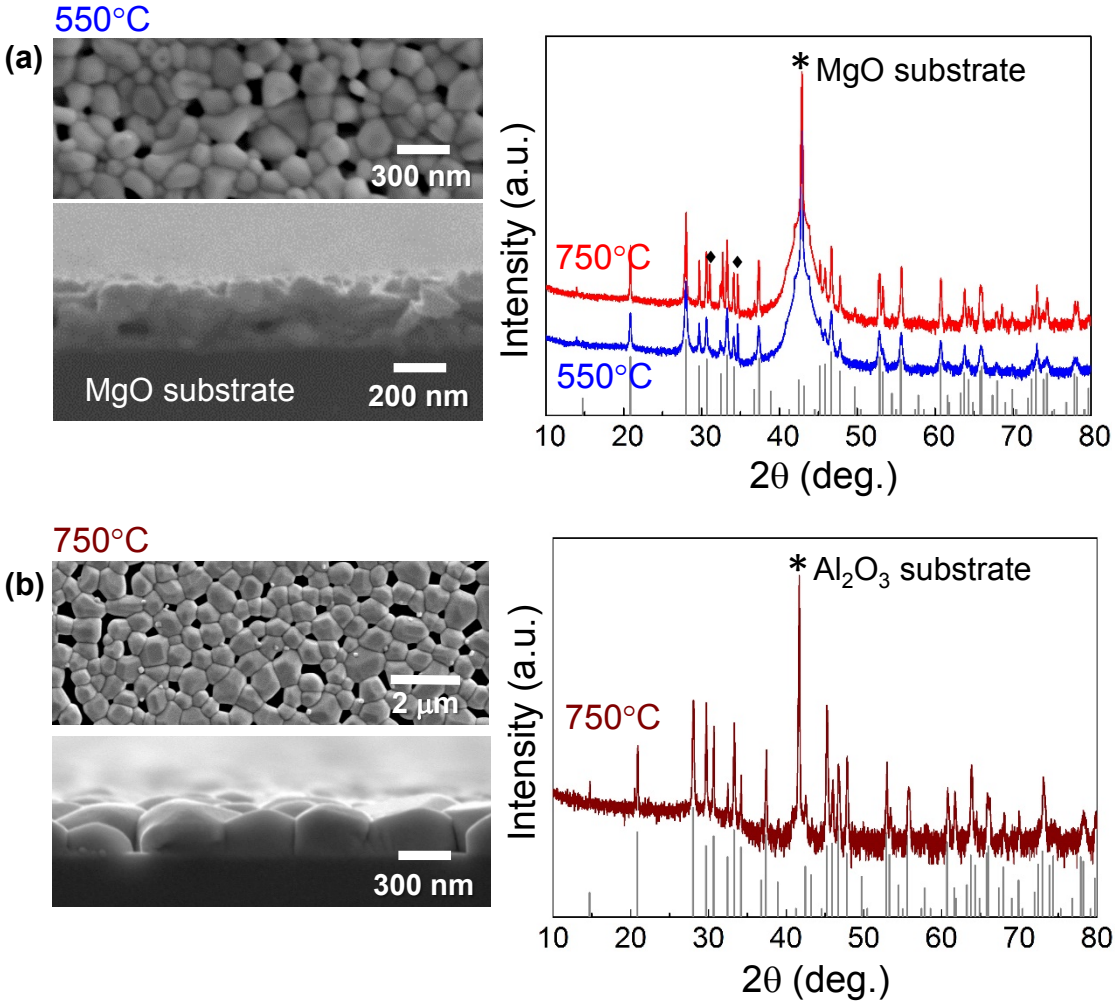

Figure S1. Polycrystalline microstructure and phase identification. Dense polycrystalline $CuBi_2O_4$ films were successfully deposited on (**a**) MgO and (**b**) Al_2O_3 substrates. X-ray diffraction analysis verifies the tetragonal $CuBi_2O_4$ phase of fabricated films. Black diamonds in the patterns in (a) denote the Bragg reflections from unidentified secondary phases. As shown in (b), no additional Bragg peaks are identified when a Al_2O_3 substrate is used instead of MgO. Therefore, this supports that the secondary phases stem from a local reaction with the MgO substrate.

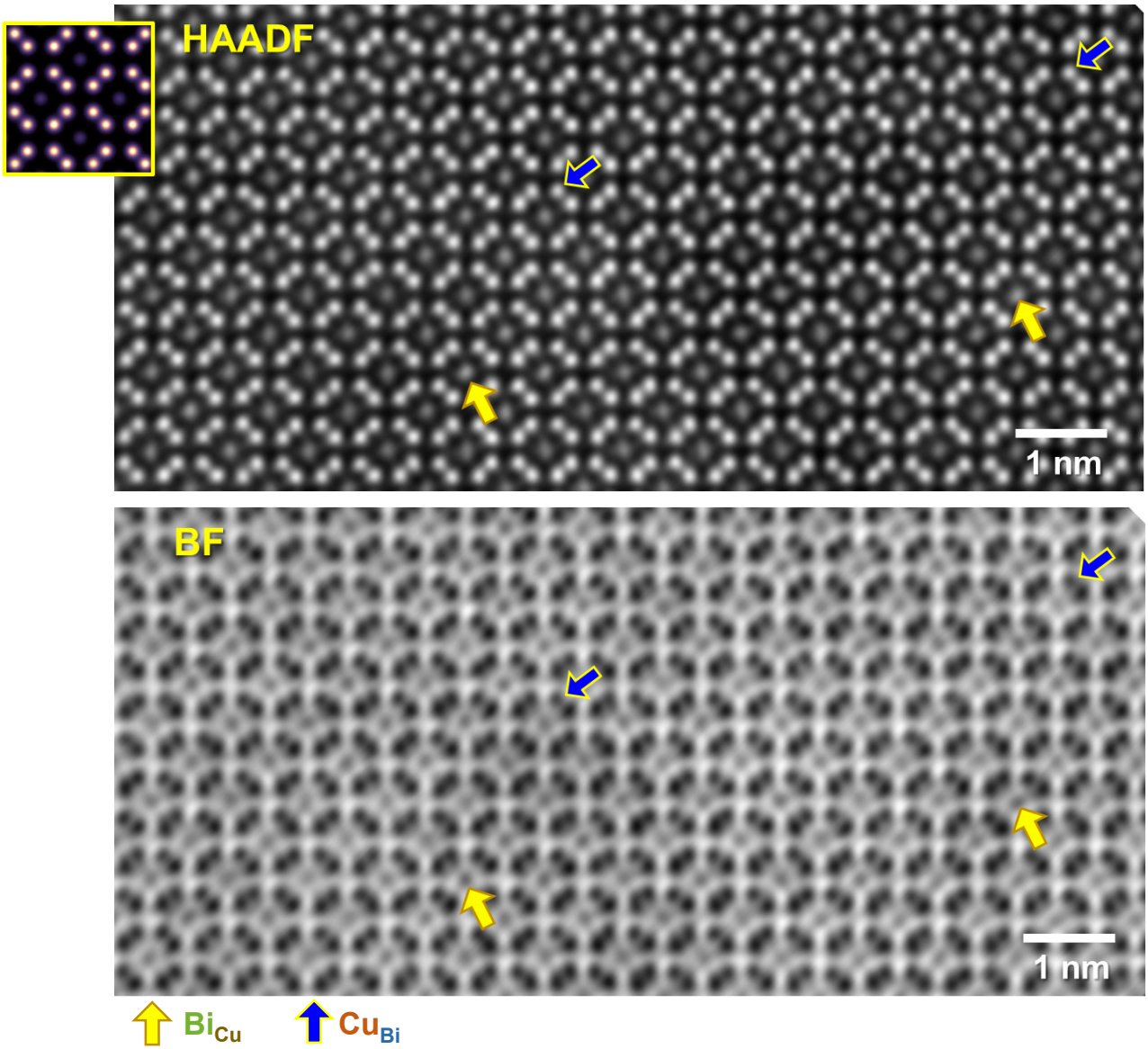

Figure S2. Pair of wide-view HAADF- and BF-STEM images in the [001] projection. Higher-intensity Cu columns are exemplified, as denoted by yellow arrows. Lower-intensity Bi columns (blue arrows) are easily identifiable in the BF image.

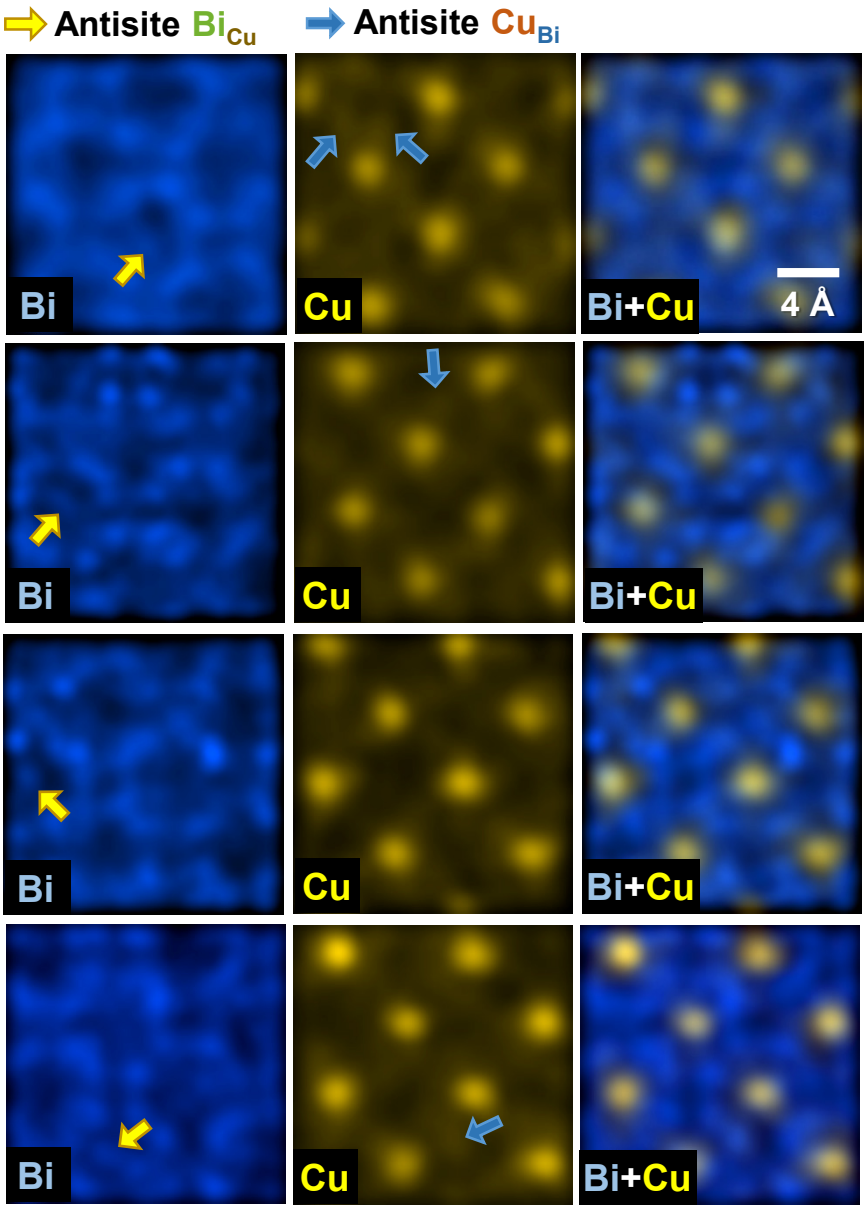

Figure S3. Additional four sets of atomic-scale composition maps by EDS. The maps were acquired in the 550°C film sample. Yellow arrows in the Bi maps indicate the presence of Bi_{Cu} antisite defects. Light blue arrows in the Cu maps also denote Cu_{Bi} antisite defects.

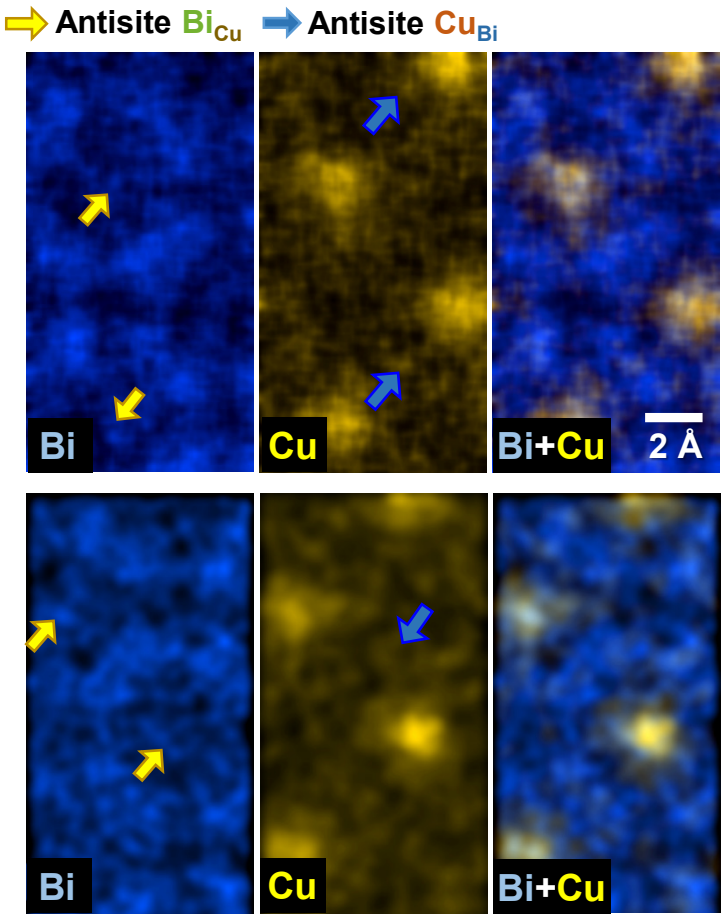

Figure S4. Additional sets of atomic-scale composition maps at a higher magnification. The maps were acquired in the 550°C film sample. These consistently show the presence of Bi_{Cu} and Cu_{Bi} aintisite intermixing, as indicated by arrows.

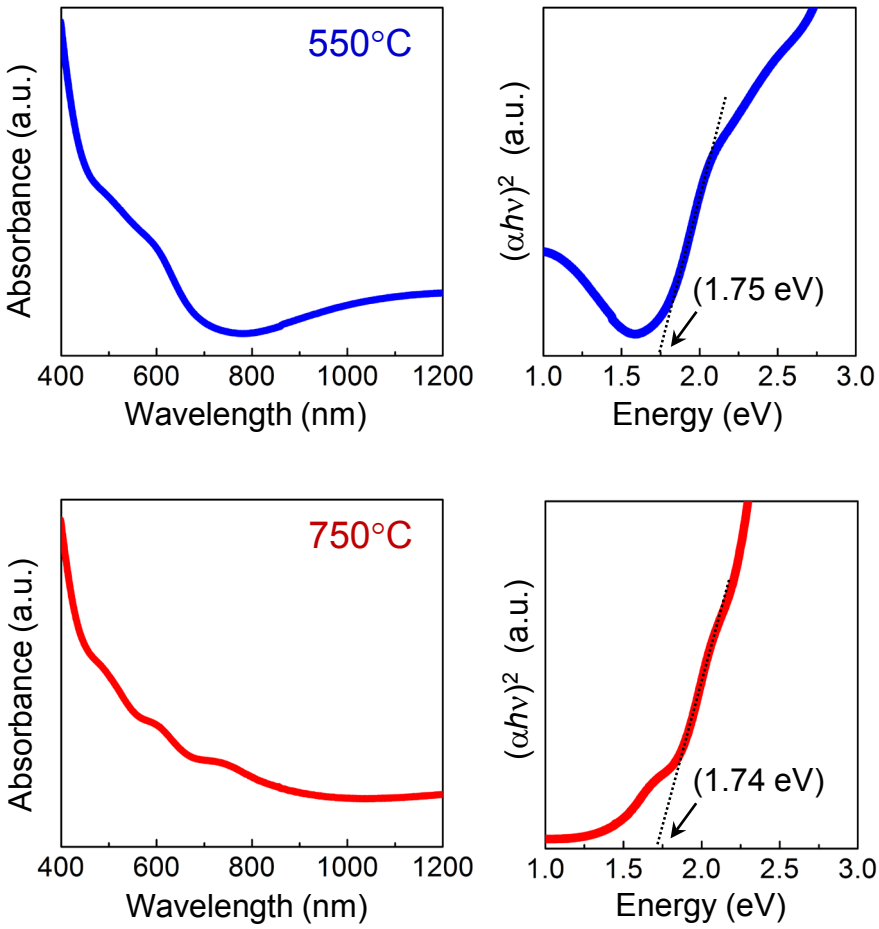

Figure S5. Optical absorbance measurements. The optical absorbance spectrum was measured for each sample in a range of 300–1400 nm (left column). The $[\alpha h\nu]^2$ values (where α is the absorption coefficient and $h\nu$ is the energy of the light) are plotted as a function of energy in the unit of eV (right column) to obtain the direct bandgap.

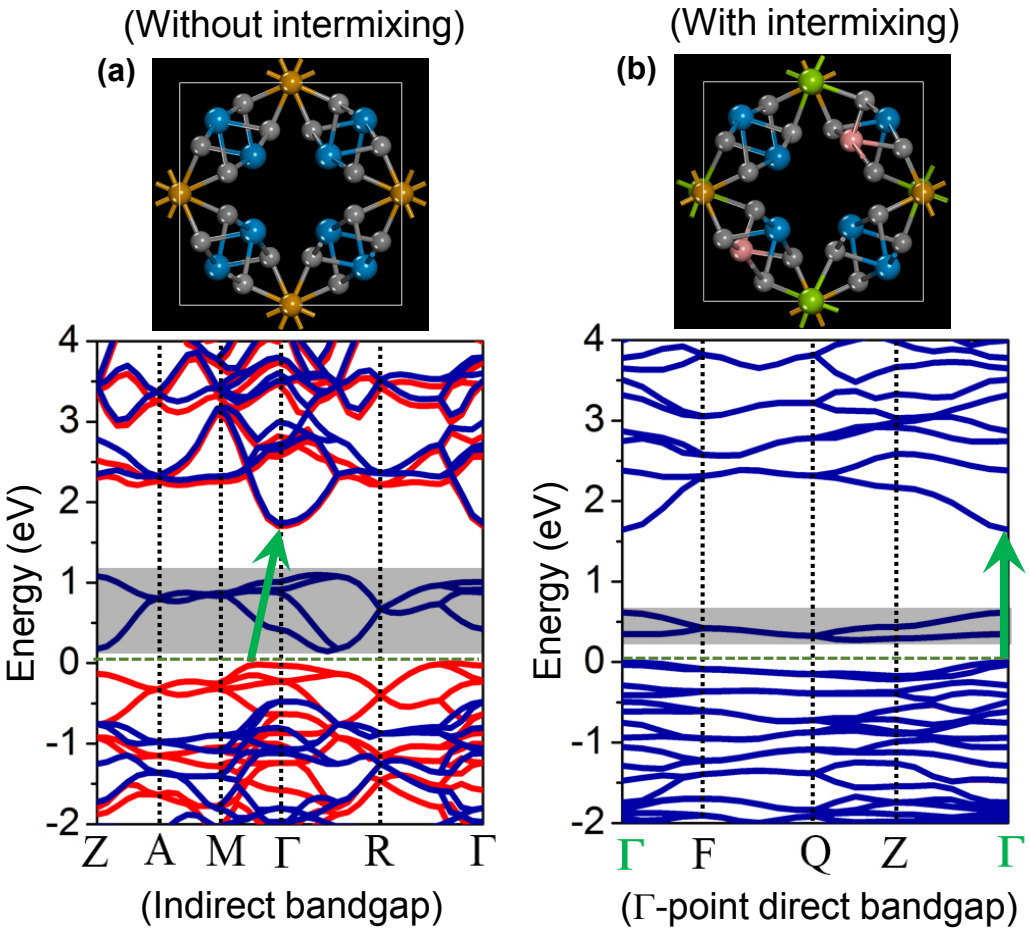

Figure S6. Bandgap characteristics. (**a**) The indirect bandgap for pristine $CuBi_2O_4$ without intermixing and (**b**) the Γ-point direct bandgap for the case of antisite intermixing are clarified on the electronic band structures by green arrows.

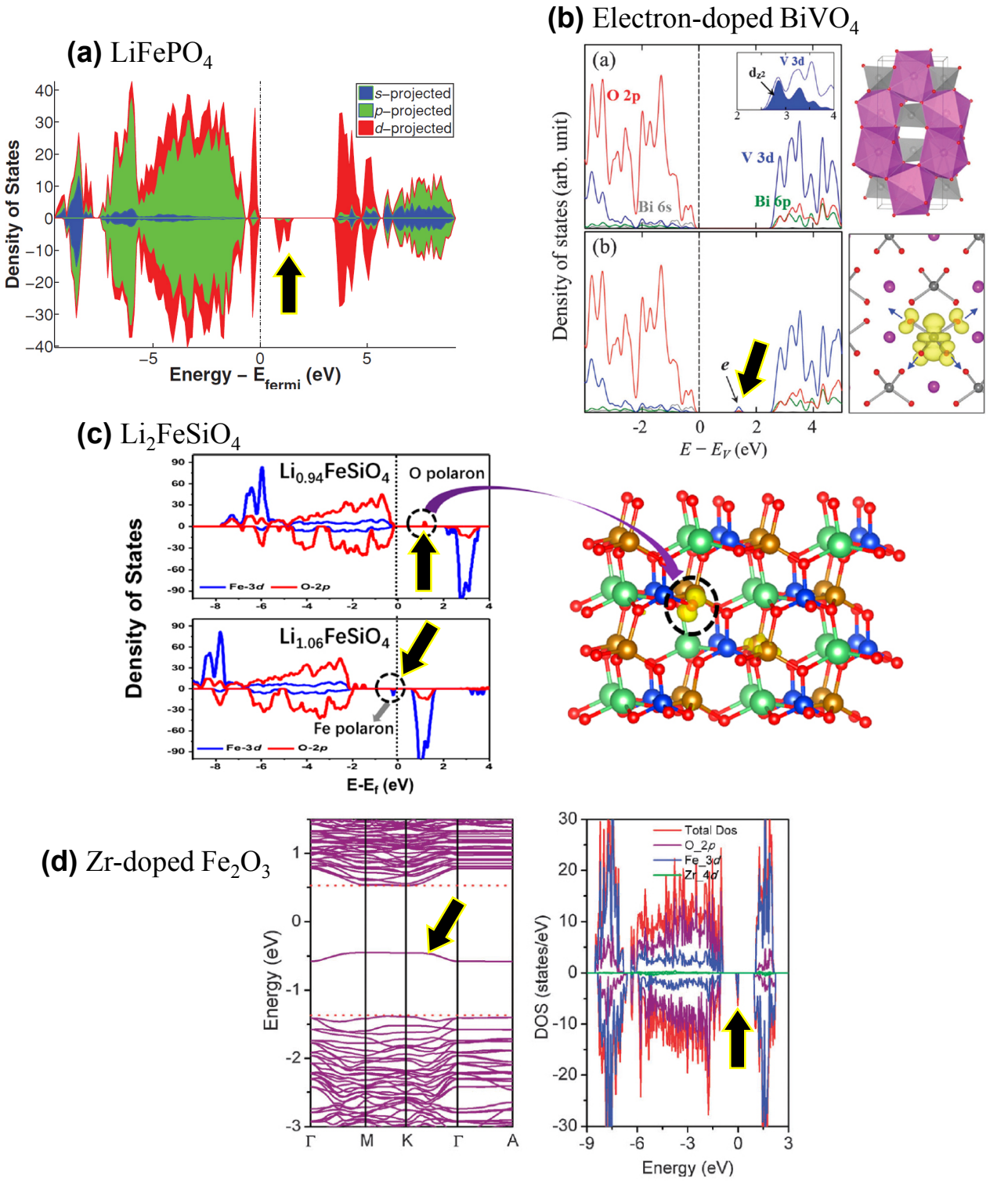

Figure S7. Examples of the DOS plot showing the local polaron states (black arrows) within the bandgap. These metal oxides are known to show conduction behavior by polaron hopping rather than band-like conduction. (**a**) $LiFePO_4$ (reproduced with permission from ref. 32; copyright 2011, The American Physical Society). (**b**) Electron-doped $BiVO_4$ (reproduced with permission from ref. 33; copyright 2015, The Royal Society of Chemistry). (**c**) Li_2FeSiO_4 (reproduced with permission from ref. 34; copyright 2018, The American Chemical Society). (**d**) Zr-doped Fe_2O_3 (reproduced with permission from ref. 35; copyright 2015, The Royal Society of Chemistry).